

Cite this article as: Wang Zeng, Zhang Zan, Liu Nannan, et al. Bending Behavior of Closed-Cell Aluminum Foam Bar with Thin Outer Wall[J]. Rare Metal Materials and Engineering, 2024, 53(03): 667-675. DOI: 10.12442/j.issn.1002-185X.20230141.

ARTICLE

Bending Behavior of Closed-Cell Aluminum Foam Bar with Thin Outer Wall

Wang Zeng¹, Zhang Zan², Liu Nannan¹, Xia Xingchuan¹, Zhang Zichen¹, Ding Jian¹, Wang Jiacheng¹, Cui Lipeng¹, Qiu Zixuan¹, Wang Yujiang⁴, Liu Yongchang³

¹ School of Materials Science and Engineering, Hebei University of Technology, Tianjin 300401, China; ² College of Physics and Electronic Engineering, Xingtai University, Xingtai 054001, China; ³ School of Materials Science and Engineering, Tianjin University, Tianjin 300350, China; ⁴ National Key Laboratory for Remanufacturing, Army Academy of Armored Forces, Beijing 100072, China

Abstract: Aluminum foam bar (AFB) with thin outer wall was prepared by melt foaming method. The effect of span, diameter and porosity on its bending deformation behavior was investigated by cantilever beam bending experiment and finite element simulation. Bending deformation behavior was recorded by high-speed camera and the relationship between load and displacement was obtained. X-ray micro-computer tomography (Micro-CT) technique based on 3D finite elements was selected to scan and to reconstruct AFB, by which numerical simulation was carried out. The results show that span has important effect on the failure behavior and the increased span leads to decreased energy absorption capacity. In addition, increased diameter and relative density contribute to peak load improvement. Finite element simulation results match well with the experimental results, which clarifies that cell walls fail due to different types of stress during the bending process. Crack propagation follows the weakest cell walls path link during the failure process.

Key words: aluminum foam bar; cantilever beam bending; failure mechanism; finite element simulation

Closed-cell aluminum foams are structural-functional integrated materials consisting of solid aluminum matrix and gaseous phase cells^[1]. Due to their special porous structures, aluminum foam has excellent comprehensive properties, such as low density, favorable energy absorption capacity, specific strength and stiffness^[2-4]. However, due to poor mechanical properties of surface monolayer cell walls, aluminum foam cannot be used directly in industrial applications. It should be processed into composite structures such as sandwich panels and filled tubes, which are used in automotive, construction and aerospace industries^[5-7]. As core material in composite structures, aluminum foam provides energy absorption, acoustic and damping properties which are unavailable to solid metals^[8-9]. Meanwhile, mechanical properties of aluminum foam composite structures depend greatly on bonding strength between solid shells and foam cores^[10-12]. During mechanical responses, loading transmission depends on interfacial bonding quality, and poor interfacial bonding

will lead to unequal stress distribution, which results easily in failure^[13]. Up to date, adhesive, welding and mechanical bonding methods are generally used to manufacture aluminum foam composite structures^[14]. These ways have low production cost and high production efficiency, while mechanical properties and service life are seriously inadequate^[14-16]. It has been proved that metallurgical bonding can provide excellent mechanical properties and long service life for aluminum foam composite structures which are prepared through secondary processing methods^[17-18]. Based on this, it is predictable to further lower production cost and to improve comprehensive performances of aluminum foam composite structure with one-step forming method, which can realize metallurgical combination between surface structure and aluminum foam interfaces.

Composite structures filled with aluminum foam bars have been increasingly used in automobile and aerospace industries^[19-21]. It not only reduces the overall mass of vehicle,

Received date: March 19, 2023

Foundation item: Military-Civilian Integration Development of Hebei Province; Key R&D Program of Hebei Province (22351003D)

Corresponding author: Xia Xingchuan, Ph. D., Professor, School of Materials Science and Engineering, Hebei University of Technology, Tianjin 300401, P. R. China, E-mail: xiaxingchuan0101@163.com

Copyright © 2024, Northwest Institute for Nonferrous Metal Research. Published by Science Press. All rights reserved.

but also retains some strength and reduces energy consumption^[22–23]. Recently, researchers have devoted to three-point bending and four-point bending tests for cylindrical aluminum foam composite structures to evaluate their service performances^[24–28]. It has been proved that aluminum foam bar filled tube possesses higher loading carrying capacity and energy absorption efficiency compared with empty tube, and stronger bending resistance is achieved with higher density of aluminum foam filler^[29]. In addition, bending behavior of aluminum foam bar filled circular steel tubes is closely related to the foam filling rate^[30]. Meanwhile, cantilever in large satellites is an important application field for aluminum foam composite materials. Aluminum foam structure may be deflected by external forces during service, reducing its service life^[31–32]. However, research on bending properties of aluminum foam structure under cantilever beam case has gaps. Research shows that geometric factors, e. g. span or loading position, can affect loading distribution and stress intensity of micro-cantilever beams^[33].

In this work, aluminum foam bars (AFBs) with thin outer walls were prepared by melt foaming method. Several samples were integrally formed by special molds. Cantilever beam bending tests were carried out and divided into two types according to the span. Effects of diameter and porosity on bending deformation behavior of AFB were investigated. Both experiment and simulation methods were adopted to evaluate the deformation behavior. Real structure of AFB based on X-ray micro-computer tomography (Micro-CT) was applied to Abaqus, which is beneficial to accurately analyze its deformation behavior and stress distribution under cantilever beam bending conditions.

1 Experiment

1.1 Preparation of AFB

AFB with thin outer wall was prepared by melt foaming method. To obtain experimental samples efficiently, the mold of AFB consisted of columnar sections with three different diameters. Commercially pure aluminum ingots (Al, with the purity of 99.5wt%) was used as raw material. 2.0wt% calcium granules (Ca, commercially pure with granularity of 1–2.5 mm), 1.8wt% TiH₂ (commercially pure, 46–52 μm) and 1.0wt% magnesium block (Mg, with purity of 99.9%) were used as thickening agent, foaming agent and wetting agent, respectively. A set of aluminum foam forming equipment with double-zone (foaming and holding) was used^[17]. Detailed preparation processes are as follows: (1) melt certain quality of Al ingot in a crucible at 720 °C, then adjust the temperature to 710 °C and hold for 15 min to stabilize the melt; (2) add 1wt% Mg with the stirring speed of 300 r/min for 5 min to reduce surface tension, and then add thickening agent into the melt with the stirring speed of 800 r/min for 5 min followed by holding for 20 min; (3) add 1.5wt%–1.8wt% TiH₂ with the stirring speed of 1100 r/min for 20 s followed by holding for 20–30 s; (4) pour the melt into a special mold which is located in the lower chamber, followed by holding at 660 °C for 30–

50 s; (5) cool the mold by forced air and then take out the AFB. Thin wall was formed on the outer surface of AFB by cooling with forced air. By regulating the coordination between temperature and time of foaming and holding processes, AFBs with uniform distribution of cells and different porosities were prepared.

1.2 Cantilever beam bending test

As shown in Fig. 1a, AFB samples with 100 mm in height and 15, 20 and 25 mm in diameter were machined by wire electrical discharge machining (WEDM). All samples used for cantilever bending experiment were identical in size. AFB sample was clamped and fixed firmly by bench clamp (Fig. 1b), and then cantilever beam bending tests were conducted on a universal testing machine (WDW-300, Jinan, China) with the maximum load of 300 kN. Two kinds of spans were applied (Fig. 1b) to investigate their effect on bending behavior of AFB. Type A ($L_A=90$ mm) and Type B ($L_B=50$ mm) represent different loading positions. All the tests were carried out under displacement control and a constant cross-head speed of 1.5 mm/min was used for the whole process at room temperature. Displacement and loading were recorded by data acquisition software installed on a personal computer. High-speed camera was used for recording macroscopic deformation process. To quantify the deformation behavior of AFB samples in cantilever beam bending test, ratio of D/L was adopted to show its macroscopic deformation degree, where L is span and D is displacement of the cross-head. In the initial state, D/L is 0 and samples have not yet been deformed in any way.

1.3 Construction of 3D geometric model

YXLON X-ray computation tomography system (YXLON International, Germany, and Institute of Mechanics, Chinese Academy of Sciences) with acceleration voltage of 120 kV, geometrical magnification of 12.35 and current of 0.59 mA was used for getting real structure of AFB. The distance from the source to sample and from sample to detector was 64.87 and 736.11 mm, respectively. As shown in Fig. 2a, a group of 1390 projects were obtained for a complete rotation of each sample with 30 μm in voxel size of 2D slice images. Distortion of external environment, device itself and image format during the conversion process can lead to the blurring of edge image. To avoid this situation, Avizo software (Thermo Fisher Scientific, USA, Tianjin Sanying Precision Instrument Co., Ltd) was selected to preprocess and to stack the original images by interactive thresholding and volume rendering module, as shown in Fig. 2b. The model of large size tends to convergence difficultly. Therefore, in this work, the original voxel was reduced to 1/5 of its original size to construct the 3D model and the models meshed. During the reconstruction of 3D model (Fig. 2c), the original image was binarized first, and then two different colors were selected for interactive threshold segmentation for clearly distinguishing the cells and cell walls of AFB samples. To simplify the 3D model and to simulate convergence, all internal cells smaller than 0.1 mm were ignored. Then the 3D model was

constructed by the project of volume rendering, and so far, 3D visualization of AFB sample was completed. 3D model (Fig. 2d) with geometric meshes of 401 158 tetrahedral elements (C3D4) was imported into Abaqus/explicit (Dassault Systèmes Simulia Corp., USA).

1.4 Finite element simulation

It has been proved that small blocks of closed-cell aluminum foam without obvious defects can exhibit similar mechanical behavior to larger aluminum foam blocks^[34-35]. In this work, to improve simulation efficiency, outer wall and internal skeleton of AFB were separated by Avizo, keeping the internal skeleton unchanged, and the sample was scaled down equivalently to 1/5 of its original size. Abaqus/explicit was used for finite element simulation. Properties of the matrix materials were characterized by Johnson-Cook (JC) model; density, Young's modulus and Poisson's ratio of the cell wall material were set to 2.7×10^{-9} t/mm², 7×10^4 MPa and 0.33, respectively^[19]. Flexible injury was used in the model, and fracture strain and failure displacement were set as 0.1 and 0.01, respectively. Cross-head was set as shell rigid body. To prevent the impact action of cross-head, coupling constraints at the contact point between the cross-head and AFB sample model were used. Boundary conditions constrain all degrees of freedom except for downward movement of bar part of AFB model. The bending behavior of AFB sample was calculated by explicit solver to ensure successful convergence of the complex cell structure deformation. Finally, contact interaction was defined at the cross-head and two positions of AFB sample model, and the friction coefficient and elastic sliding of tangential were set as 0.01 and 0.005, respectively.

2 Results and Discussion

2.1 Deformation process analysis

Fig. 3 and Fig. 4 show the bending progress of Type A and Type B samples, respectively, which can reflect the general deformation progress of AFB with different diameters (15, 20, 25 mm). It can be seen that AFBs with different spans and diameters possess similar deformation processes, that is, they do not deform like elastic materials. When the loading process begins, turning angle and deflection of AFB samples grow accordingly. When D/L reaches a

certain value, obvious cracks appear near the upper part of bottom outer wall, which are marked by yellow dashed squares. Then cracks spread downwards until the sample loses its bearing capacity. However, due to the cross-head closer to the fixed end, cracks sprout earlier for Type B condition under the same compression rate. In addition, the lower part of outer cell wall away from cross-head shows minor wrinkle due to compressive stress (marked by white dashed squares).

To analyze the macroscopic deformation behavior, the bending moment equation for a cantilever beam is used:

$$M_c = FL \quad (1)$$

where M_c (N·m) is moment of force, F (N) is the load and L (m) is the span. It can be obtained that moment increases with increasing span. Therefore, moment near the bottom is larger, which should be the reason for cracks appearing on the upper part of bottom. D/L values will be different for each sample when the samples fail due to the differences in cell structure or location of budding cracks. In the region with relatively higher moment, cracks occur in cell walls where limiting tensile stress will be reached earlier. Due to its brittleness and lower strength, AFB shows almost no obvious indentation at the point of cross-head contacted^[36]. After cracks appear, the cracks expand rapidly through the thin sections of cell walls along with microcracks until it fails^[37]. For the failure section, tensile load appears on the upper surface, and compressive load appears on the bottom surface^[38-39].

2.2 Cantilever beam bending performances

2.2.1 Load-displacement characteristics

Fig. 5 shows the load-displacement curves of Type A AFB samples with different diameters and porosities. It is clear that the deformation process can be divided into two stages, that is, elastoplastic stage (section I) and failure stage (section II). Within section I, AFB experiences elastic and plastic deformations, the load increases with increasing displacement until local failure occurs. In section II, the load decreases sharply with increasing displacement. Fig. 6 shows the load-displacement curves of Type B AFB. Different from Type A, they can be divided into three stages, that is, linear elastic stage (section I), plastic plateau stage (section II) and failure stage (section III). In section I, peak load reaches within a shorter displacement due to the cross-head closer to the

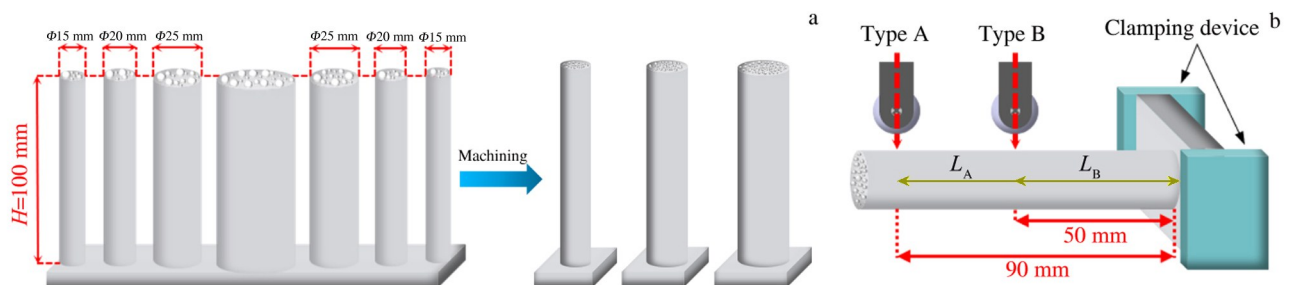


Fig.1 Schematic diagrams of cantilever beam bending test: (a) integral formed AFB and post-processing samples and (b) bending experiment for Type A and Type B samples

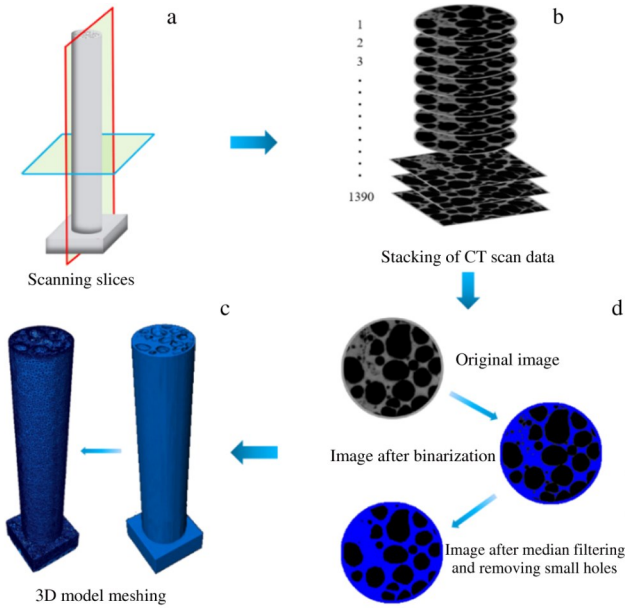


Fig.2 Real 3D model reconstruction process

bottom of AFB. Afterward, with increasing the displacement, a plateau stage appears where cracks continue to expand downward.

For Type A condition, peak load was defined as the first peak value on load-displacement curves. While, for Type B case, the average value of plateau stage in the load-displacement curve was defined as the peak load. Fig.5a–5c and Fig.6a–6c show AFB samples with the same diameter and different porosities of ~60%, ~70% and ~80%. To clarify the relationship between porosity and peak load, take Fig.6a for example, it can be seen that the peak load decreases with increasing porosity. Meanwhile, similar results can be

found in Fig.6b – 6c and Fig.5b – 5c. This means that the bending strength of AFB decreases with increasing porosity regardless of span. The reason for this phenomenon is that most of the load is borne by the cell walls, and as load increases, stress destruction occurs in the cell walls because stress is concentrated, resulting in cracks. Stress destruction occurs as the load continues, which leads gradually to the failure of the entire sample^[40–41]. Generally, samples with low porosity have thicker cell walls, which increase the strength of the foams. In addition, samples with low porosity have more metal skeletons due to lower cell content. When the load exceeds load-bearing capacity of the skeleton, sample with lower porosity will further resist stress, resulting in higher yield strength at macro level^[42]. Meanwhile, thin outer walls of AFB provide a complete skin structure that further enhances the yield strength compared with aluminum foam.

Besides porosity, diameter also affects the flexural resistance of AFB (Fig.7 and Fig.8). For Type A AFB with porosity of 60%, peak load increases by 29.5% when diameter increases from 15 mm to 25 mm. For samples with porosity of 70% and 80%, the peak loads increases by 40.9% and 33.1%, respectively. Similar results are obtained for Type B AFB (Fig.8), and samples with 15, 20 and 25 mm in diameters show peak load values of 61.15–105.27, 72.97–118.18 and 80.01–135.33 N, respectively. The reason for this is that when the porosity remains constant, increasing the diameter means increasing the number of cell walls which carry the load in radial section, leading to increased flexural strength. Furthermore, from the structural mechanics point of view, according to the cantilever beam deflection curve, Eq.(2) and Eq.(3) can be obtained^[43]:

$$I = \frac{\pi d^4}{64} \tag{2}$$

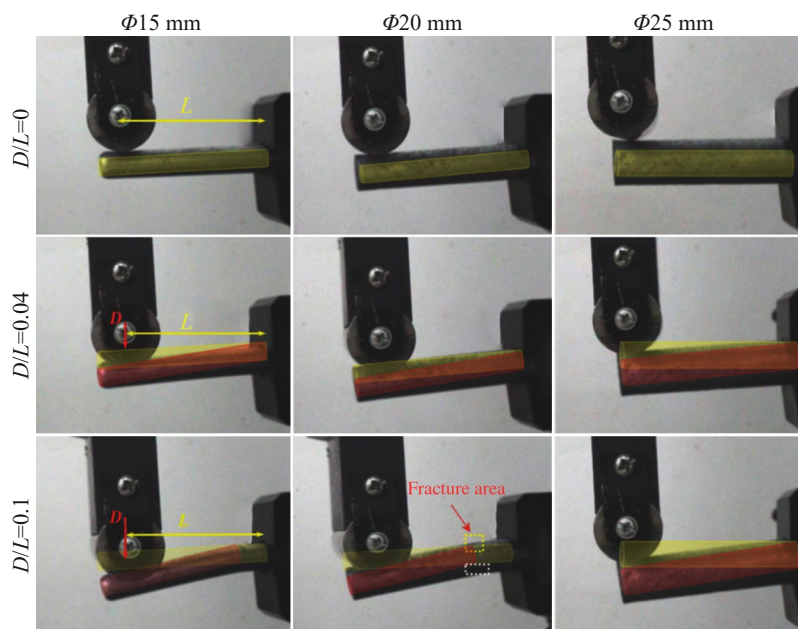


Fig.3 Macroscopic deformation and failure process of AFB under Type A condition

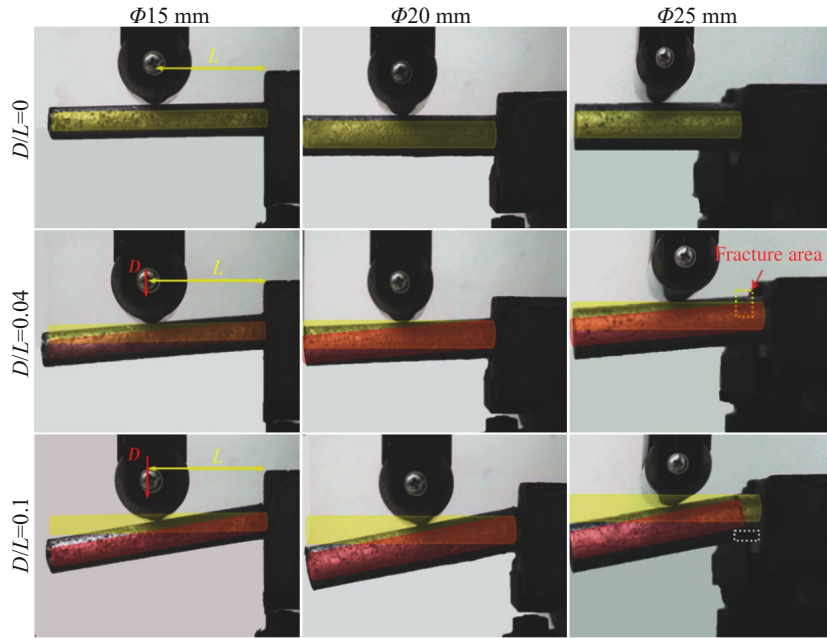


Fig.4 Macroscopic deformation and failure process of AFB under Type B condition

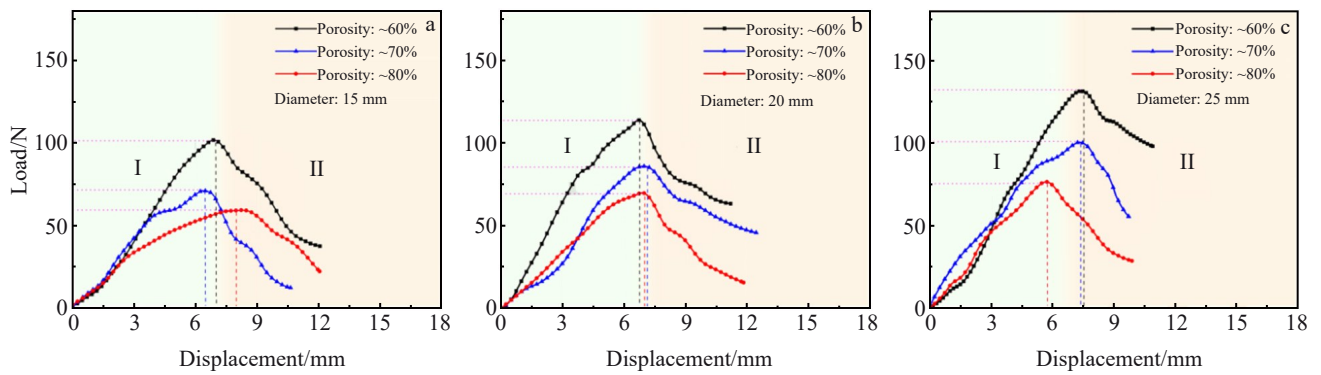


Fig.5 Load-displacement curves of Type A AFB with different diameters: (a) 15 mm, (b) 20 mm, and (c) 25 mm

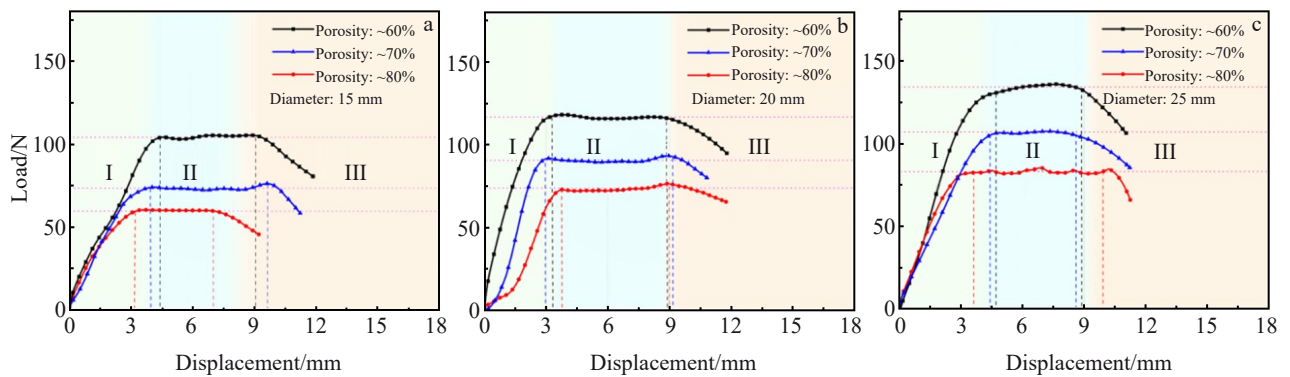


Fig.6 Load-displacement curves of Type B AFB with different diameters: (a) 15 mm, (b) 20 mm, and (c) 25 mm

$$f = \frac{FL}{6EI} (3H - L) \quad (3)$$

where I is the inertial interface moment (m^4), d is the diameter of AFB (m), f is the deflection (m), F is the load

(N), L is the span (m), E is the elastic modulus (Pa) and H is the length of AFB (m). Deflection is displacement of the center point of AFB's free end section in vertical direction, so displacement of the cross-head is proportional to the

deflection. According to Eq.(2) and Eq.(3), the load increases with increasing the diameter of AFB for the same deflection. Therefore, from the structural mechanics view point, flexural strength increases with increasing the diameter of AFB.

2.2.2 Effective energy absorption capacity

Excellent energy absorption performance allows closed-cell aluminum foams to be used in numerous applications^[42]. Therefore, it is important to evaluate the energy absorption capacity of AFB and to figure out its influencing factors. Generally, effective energy absorption capacity of AFB under cantilever beam bending can be calculated by Eq.(4)^[30]:

$$W_{ef} = \int_0^{\delta_{ef}} F(\delta) d\delta \quad (4)$$

where F is the load (N) and δ is the displacement (mm). Effective energy absorption capacity (W_{ef}) represents the total energy absorbed during effective bending stroke (δ_{ef}). The upper limit of integral is the beginning of failure stage and the lower limit is zero. As shown in Fig.7 and Fig.8, for a constant diameter of AFB, with increasing the porosity, the effective energy absorption capacity decreases. When the porosity is constant, increase in the diameter implies that there are more cells to absorb deformation energy and more space for plastic deformation^[42].

2.3 Finite element simulation analysis

After bending, the fracture of AFB generally exhibits an

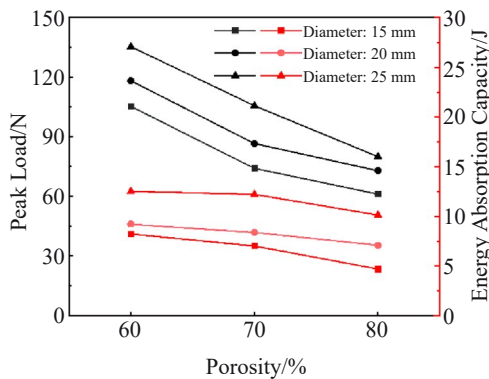


Fig.7 Effect of porosity on peak load and energy absorption capacity of Type A AFB

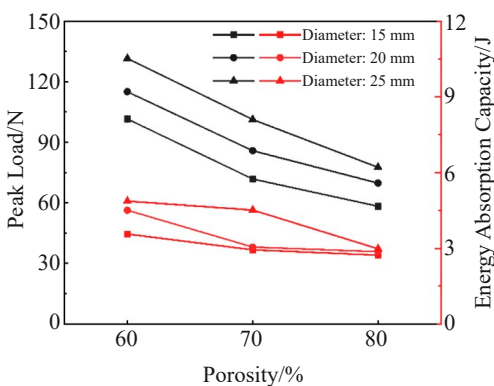


Fig.8 Effect of porosity on peak load and energy absorption capacity of Type B AFB

irregular and uneven section. Due to the outer wall, deformation of cell walls within AFB cannot be observed at the macroscopic scale. Therefore, finite element method was applied to investigate the formation of irregular fracture, stress distribution and failure process of cell walls.

Fig. 9 shows the finite element simulation results of AFB under Type A conditions. It can be seen that in the initial state, internal cell structures are not deformed and cell walls are intact and unbroken. As the deformation progresses (Fig.9b), stress concentration occurs in two regions, that is, lower part of outer wall which possesses the highest moments and cell walls subjected to shear stress, as shown by blue and green dashed square in Fig.9b. Meanwhile, as shown in Fig.9c, with the deformation process progressing, fracture occurs on internal cell walls, which leads to a rapid drop in load-displacement curve after peak load instead of plateau stage that generally exists in aluminum foam bending process. After that, fracture area forms (Fig.9d) and cracks move in an irregular way from one cell wall to another. This is because crack propagation follows the path of the weakest cell wall link^[24,37].

Fig. 10 illustrates the finite element simulation results of Type B AFB. As shown in Fig.10a and 10b, before the failure of cell walls, stress distribution is similar to that of Type A AFB. However, Type B shows different failure sequences of cell walls (Fig. 10c), the upper outer wall subjected to tensile stress fails firstly and then cracks tend to expand towards cell walls which are subjected to shear stress. With the bending process progressing (Fig. 10d), fracture area extends toward the cell walls with stress concentration, as predicted by the black line in Fig. 10c. As described above, when the deformation begins, stresses are mainly distributed in the upper and lower outer cell walls where the maximum moment exists. As D/L increases, stresses concentration gradually spreads from outside to inside.

For quasi-static compression, local deformation is affected by span. When the span is longer, chances of local deformation and its propagation in foam bar become prominent^[44].

Different local deformations result in different failure sequences of cell walls. For Type A AFB, when cell walls under shear stress fail, cell walls subjected to tensile stress are still in plastic deformation stage (Fig.9c). Although Type B AFB has opposite failure sequence (Fig.10c), cell walls subjected to tensile stress will fail firstly. It can be seen that local deformation and failure mode of AFB under cantilever beam bending are affected by the span. Combined with load-displacement curves, span has a prominent effect on failure mode.

During the deformation process, stress distribution determines the onset and propagation of cell walls failure. Meanwhile, failure of cell wall also depends on the limiting stress associated with cell walls which may be subjected to tensile, shear and mixed stresses. Cell walls exceeding its limiting stress will break down. When the neighboring cell walls reach their limiting stress and fail, the crack will also be propagated through them. Due to the dominant effect of tensile and shear stresses, plastic hinge is difficult to appear

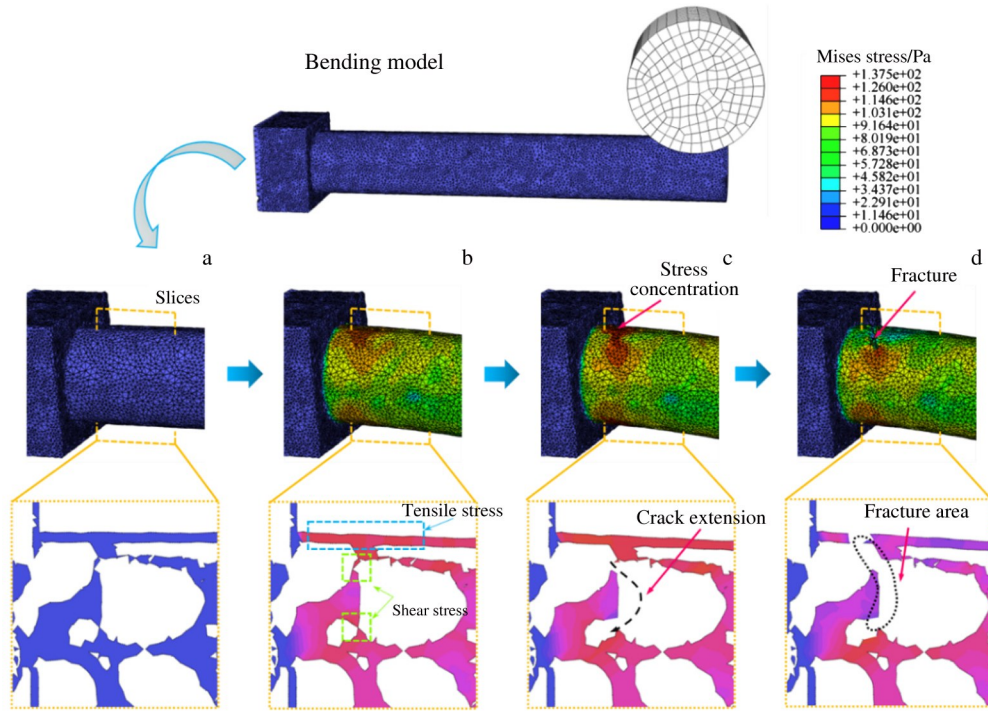


Fig.9 Failure mechanisms of Type A AFB cell walls: (a) original, (b) $D/L=0.044$, (c) $D/L=0.67$, and (d) $D/L=0.1$

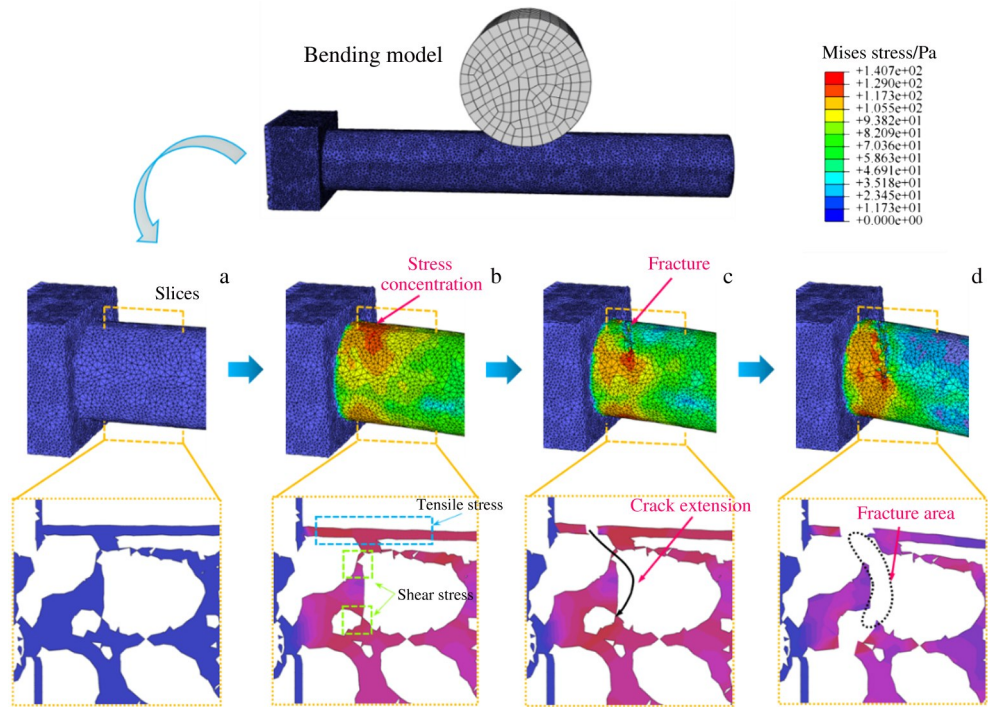


Fig.10 Failure mechanisms of Type B AFB cell walls: (a) original, (b) $D/L=0.05$, (c) $D/L=0.1$, and (d) $D/L=0.15$

in the cell walls of the fracture area. In addition, stress distribution changes with deformation process, and crack propagation occurs layer by layer, eventually resulting in the formation of an irregular fracture area and AFB bending failure. Moreover, stress distribution on outer walls determines the effective energy absorption and load-bearing capacity. Therefore, general aluminum foam without outer wall

structure deforms and fails more easily under radial load. Crack propagation paths of both Type A and Type B AFBs all extend along the weakest part of cell walls. Generally, cell walls pass different thicknesses; after the thinner and weaker cell walls fail, thicker cell walls form new weak point; failure occurs as the deformation process progresses^[17]. When the crack passes through a cell wall, any cell neighboring may

become the direction of crack propagation^[38]. Therefore, crack propagation does not occur in straight line^[45-46].

3 Conclusions

1) For Type A aluminum foam bar (AFB) samples, failure process can be divided into two stages: elastic-plastic stage and failure stage. While, for Type B samples, the deformation process can be divided into elastic stage, plastic plateau stage and failure stage. For longer span, propagation of local deformation is prominent which leads to different failure sequences of cell walls. Under Type A condition, cell walls inside the sample subjected to shear stress will fail before the outer walls subjected to tensile stress, and opposite failure sequence of cell walls occurs under Type B condition. This results in different trends of load-displacement curves.

2) Peak load and effective energy absorption capacity increase with decreasing porosity and increasing diameter, which results in thicker cell walls and more metal skeletons to resist deformation, and thus increases more space for plastic deformation. Combined with finite element analysis, cracks occur at the area with maximum moment, and failure of cell walls is related to stress distribution and limiting stress. Cell walls endure tensile, shear and mixed stresses. Cell walls exceeding its limiting stress will break down, and thinner and weaker walls induce the propagation of cracks, leading to the propagation of crack in nonlinear line. Such propagation of crack occurs layer by layer so the fracture generally exhibits irregular and uneven section.

References

- Banhart J. *Progress in Materials Science*[J], 2001, 46(6): 559
- Idris M I, Vodenitcharova T, Hoffman M. *Materials Science and Engineering A*[J], 2009, 517(1-2): 37
- Muchhala D, Yadav B N, Kumar R et al. *Composites Part B*[J], 2019, 176: 107304
- Xia X C, Chen X W, Zhang Z et al. *Materials & Design*[J], 2014, 56: 353
- Banhart J, Seeliger H W. *Advanced Engineering Materials*[J], 2012, 14(12): 1082
- Andrews E, Sanders W, Gibson L J. *Materials Science and Engineering*[J], 1999, 270(2): 113
- Zhang Z C, Liu N N, Zhang Z et al. *International Journal of Mechanical Sciences*[J], 2023, 242: 108039
- Banhart J, Seeliger H W. *Advanced Engineering Materials*[J], 2008, 10(9): 793
- Mohan K, Hon Y T, Idapalapati S et al. *Materials Science and Engineering A*[J], 2005, 409(1-2): 292
- Crupi V, Montanini R. *International Journal of Impact Engineering*[J], 2007, 34(3): 509
- He W, Lu S, Yi K et al. *International Journal of Mechanical Sciences*[J], 2019, 161-162: 105026
- Latour M, D'Aniello M, Landolfo R et al. *Thin-Wall Structures*[J], 2021, 164: 107894
- Schwingel D, Seeliger H W, Vecchionacci C et al. *Acta Astronautica*[J], 2007, 61(1-6): 326
- Lin H, Luo H J, Huang W Z et al. *Journal of Materials Processing Technology*[J], 2016, 230: 35
- Harte A M, Fleck N A, Ashby M F. *Advanced Engineering Materials*[J], 2000, 2(4): 219
- Hao Q X, Qiu S W, Hu Y B. *Rare Metal Materials and Engineering*[J], 2015, 44(3): 548
- Zhang Z C, Feng H M, Xu T et al. *Composite Structures*[J], 2022, 283: 115090
- Wang N Z, Noack M A, Kamm P H et al. *Advanced Engineering Materials*[J], 2021, 23: 2100795
- Xu T, Zhang Z C, Ding J et al. *Journal of Iron and Steel Research International*[J], 2023, 30: 392
- Chen C, Harte A M, Fleck N A. *International Journal of Mechanical Sciences*[J], 2001, 43(6): 1483
- Zhang Z, Ding J, Xia X C et al. *Material & Design*[J], 2015, 88: 359
- Islam M A, Brown A D, Hazell P J et al. *International Journal of Impact Engineering*[J], 2018, 114: 111
- Castanie B, Bouvet C, Ginot M. *Composite Part C*[J], 2020, 1: 100004
- Wang M, Yu X, Zhang J et al. *Composite Structures*[J], 2022, 280: 114873
- Yu J, Wang E, Li J et al. *International Journal of Impact Engineering*[J], 2008, 35(8): 885
- Mei J, Liu J, Huang W. *Composite Structures*[J], 2022, 284: 115206
- Sha J B, Yip T H, Teo M H. *Progress in Natural Science: Materials International*[J], 2011, 21(2): 127
- Styles M, Compston P, Kalyanasundaram S. *Composite Structures*[J], 2008, 86(1-3): 227
- Duarte I, Vesenjak M, Krstulović -Opara L. *Composite Structure*[J], 2014, 109: 48
- Zhang B, Zhang J, Wang L et al. *Engineering Structures*[J], 2021, 243: 112650
- Castanié B, Barrau J J, Jaouen J P. *Composite Structures*[J], 2002, 55(3): 295
- Deng J, Peng A, Chen W et al. *Journal of Sandwich Structures & Materials*[J], 2020, 23(6): 1870
- Mathews N G, Mishra A K, Jaya B N. *Theoretical and Applied Fracture Mechanics*[J], 2021, 115: 103069
- Jeon I, Asahina T. *Acta Materialia*[J], 2005, 53(12): 3415
- Toda H, Ohgaki T, Uesugi K et al. *Metallurgical and Materials Transactions A*[J], 2006, 37(4): 1211
- Pandey A, Muchhala D, Kumar R et al. *Composite Part B*[J], 2020, 183: 107729
- Raza M S, Datta S, Saha P. *Materials Science and Engineering A*[J], 2021, 809: 140907
- Zhou J, Hassan M Z, Guan Z W et al. *Composite Science and Technology*[J], 2012, 72(14): 1781

- 39 Sun Z, Jeyaraman J, Sun S Y et al. *Composite Science and Technology*[J], 2012, 43(11): 2059
- 40 Wang H, Zhou X Y, Long B et al. *Materials Science and Engineering*[J], 2013, 582: 316
- 41 Liu J, Qu Q X, Liu Y et al. *Journal of Alloys and Compounds*[J], 2016, 676: 239
- 42 Yan C, Song X, Zhu H et al. *Journal of Composite Materials*[J], 2017, 52(14): 1887
- 43 Matsuzaki J, Ishiyama C. *Microelectronic Engineering*[J], 2013, 110: 108
- 44 McCormack T M, Miller R, Kesler O et al. *International Journal of Solids and Structures*[J], 2001, 38(28–29): 4901
- 45 Hartmann J, Trepper A, Korner C. *Advanced Engineering Materials*[J], 2011, 13(11): 1050
- 46 Bang S O, Cho J U. *International Journal of Precision Engineering and Manufacture*[J], 2015, 16(6): 1117

具有薄外壁的闭孔泡沫铝棒的弯曲行为

王 增¹, 张 赞², 刘楠楠¹, 夏兴川¹, 张子晨¹, 丁 俭¹, 王佳成¹, 崔李鹏¹, 邱子轩¹, 王玉江⁴, 刘永长³

(1. 河北工业大学 材料科学与工程学院, 天津 300401)

(2. 邢台学院 物理与电子工程学院, 河北 邢台 054001)

(3. 天津大学 材料科学与工程学院, 天津 300350)

(4. 陆军装甲兵学院 装备再制造技术国防科技重点实验室, 北京 100072)

摘 要: 通过熔融发泡法制备了具有薄外壁的铝泡沫棒 (aluminum foam bar, AFB)。通过悬臂梁弯曲实验和有限元模拟研究了跨度、直径和孔隙率对其弯曲变形行为的影响。采用高速摄像机记录了 AFB 的弯曲变形行为, 并得到了载荷和位移之间的关系。基于三维有限元的 X 射线微断层扫描技术 (Micro-CT) 重建 AFB, 并进行了数值模拟。结果表明, 跨度对破坏行为有重要影响, 跨度的增加导致了能量吸收能力下降。此外, 直径和相对密度的增加也使得峰值载荷提高。有限元模拟结果与实验结果相吻合, 这说明孔壁在弯曲过程中由于不同类型的应力而失效。在失效过程中, 裂纹遵循孔壁最薄弱的路径传播。

关键词: 泡沫铝棒; 悬臂梁弯曲; 失效机制; 有限元模拟

作者简介: 王 增, 男, 1997年生, 硕士, 河北工业大学材料科学与工程学院, 天津 300401, E-mail: 18222875258@163.com